

See discussions, stats, and author profiles for this publication at: <https://www.researchgate.net/publication/51903587>

One-Dimensional Corrugation of the h-BN Monolayer on Fe(110)

ARTICLE in LANGMUIR · DECEMBER 2011

Impact Factor: 4.46 · DOI: 10.1021/la2035642 · Source: PubMed

CITATIONS

26

READS

53

7 AUTHORS, INCLUDING:



[A. A. Zakharov](#)

Lund University

136 PUBLICATIONS 2,047 CITATIONS

[SEE PROFILE](#)



[Anders Mikkelsen](#)

Lund University

156 PUBLICATIONS 2,795 CITATIONS

[SEE PROFILE](#)



[Edvin Lundgren](#)

Lund University

231 PUBLICATIONS 5,798 CITATIONS

[SEE PROFILE](#)



[Alexei Preobrajenski](#)

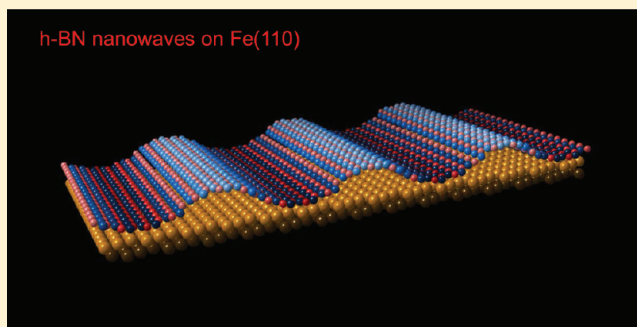
Lund University

89 PUBLICATIONS 1,680 CITATIONS

[SEE PROFILE](#)

One-Dimensional Corrugation of the *h*-BN Monolayer on Fe(110)N. A. Vinogradov,^{†,‡} A. A. Zakharov,[‡] M. L. Ng,^{†,‡,⊥} A. Mikkelsen,[§] E. Lundgren,[§] N. Mårtensson,[†] and A. B. Preobrajenski^{*,‡}[†]Department of Physics and Astronomy, Uppsala University, Box 530, 75121 Uppsala, Sweden[‡]MAX-lab, Lund University, Box 118, 22100 Lund, Sweden[§]Division of Synchrotron Radiation, Institute of Physics, Lund University, Box 118, 22100 Lund, Sweden

ABSTRACT: We report on a new nanopatterned structure represented by a single atomic layer of hexagonal boron nitride (*h*-BN) forming long periodic waves on the Fe(110) surface. The growth process and the structure of this system are characterized by X-ray absorption (XAS), core-level photoemission spectroscopy (CL PES), low-energy electron microscopy (LEEM), microbeam low-energy electron diffraction (μ LEED), and scanning tunneling microscopy (STM). The *h*-BN monolayer on Fe(110) is periodically corrugated in a wavy fashion with an astonishing degree of long-range order, periodicity of 2.6 nm, and the corrugation amplitude of ~ 0.8 Å. The wavy pattern results from a strong chemical bonding between *h*-BN and Fe in combination with a lattice mismatch in either $[\bar{1}11]$ or $[1\bar{1}1]$ direction of the Fe(110) surface. Two primary orientations of *h*-BN on Fe(110) can be observed corresponding to the possible directions of lattice match between *h*-BN and Fe(110), with approximately equal area of the boron nitride domains of each orientation.



■ INTRODUCTION

The continuous trend of device miniaturization stimulates the search for self-assembling nanostructures applicable in industry. In particular, it is highly attractive to complement the traditional “top-down” methods in fabrication of nanopatterned substrates with the new “bottom-up” techniques.¹ One of the promising routes toward self-organized templates is the formation of strongly corrugated monolayers of sp^2 -bonded materials, such as hexagonal boron nitride (*h*-BN)^{2–11} and graphene^{9,12–23} on lattice-mismatched transition metal substrates. When grown on close-packed lattice-mismatched substrates with hexagonal symmetry, the monolayers of *h*-BN or graphene can form long-range areas with the periodic muffin-tin-like corrugation in two dimensions (2D), often referred to as “nanomesh”.^{4,5,11} The corrugation amplitude is determined by the strength of interaction between the monolayer and the substrate.^{7,8,11} The resulting 2D-periodic nanotemplates can be used for a controllable growth, ordering and immobilization of large molecules,^{2–4} and arrays of metal clusters with a very narrow size distribution.^{12,16,23–25}

In addition to the perfect periodicity on the nanometer scale, the *h*-BN- and graphene-based patterned templates are chemically inert and thermally stable, thus being usable at ambient pressure conditions.^{3–5,12,16} For this reason they are attractive for catalysis or device fabrication applications. However, the nanoscaled objects like metal and semiconductor clusters, large molecules, and molecular aggregates can be assembled on the nanomesh templates only as zero-dimensional (0D) objects because of the characteristic “muffin-tin”

potential relief. The question arises whether it is possible to use the high elasticity of the *h*-BN and graphene monolayers to force them to oscillate not in two but only in one crystallographic direction, thus forming wavy patterns. Obviously, robust templates with high-precision profiling capable of ordering atoms and molecules in long chains are highly interesting for the research of structural and electronic properties in one-dimensional (1D) objects.

Here we demonstrate that it is possible to utilize the elasticity of the sp^2 -bonded materials and form long and periodic 1D nanowaves using the growth of an *h*-BN monolayer on the Fe(110) surface as an example. Prior to our study, a formation of 1D *h*-BN-based structures via utilization of pseudohexagonal symmetry of the (110) substrate surfaces of bcc metals was reported for *h*-BN on Mo(110)²⁶ and *h*-BN on Cr(110).²⁷ One-dimensional *h*-BN-derived structures were also observed on (110) surfaces of fcc materials such as Pd²⁸ as a result of specific orientation of *h*-BN in respect to the metallic substrate due to the weak interfacial bonding between *h*-BN and Pd(110) surface. However, it is highly desirable to exert better control over the resulting *h*-BN 1D structures in terms of increasing stripe length and corrugation amplitude, decreasing defect density and improving stripe periodicity. In the present study, the Fe(110) surface is chosen as a substrate because of the expected strong interaction with *h*-BN and the possibility to

Received: September 12, 2011

Revised: December 16, 2011

Published: December 21, 2011

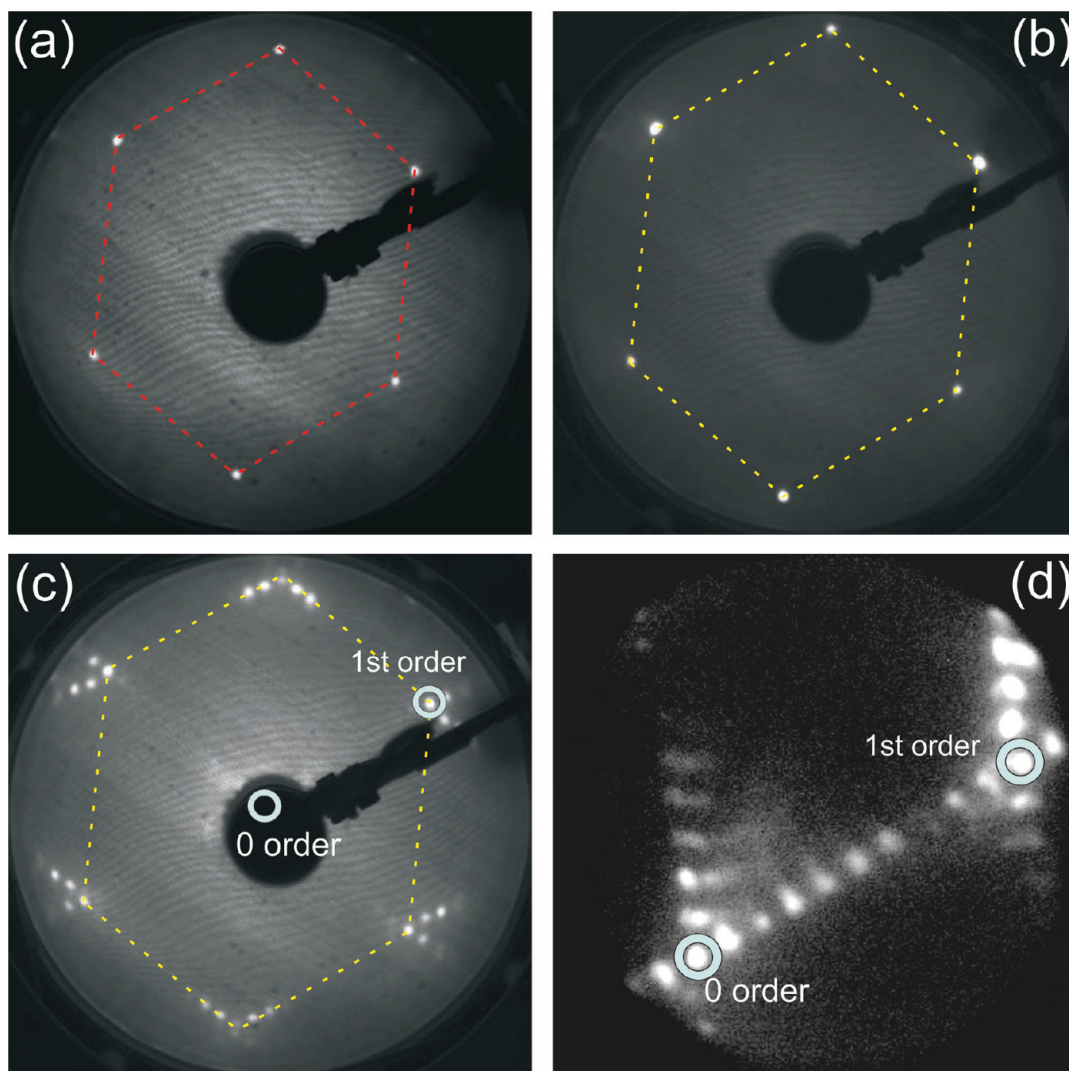


Figure 1. LEED patterns from the clean tungsten substrate (a), iron film (b), and *h*-BN/Fe/W(110) sample (c, d). The energy of the incident electron beam is 61 eV for (a), (b), and (c). Photograph (d) is a micro-LEED (μ LEED) pattern from the sample area of $\sim 1.5 \mu\text{m}$ diameter, showing the bright spots of zero and first order of diffraction and a number of additional reflexes in between, representing the moiré structure formed by the *h*-BN adlayer on the lattice-mismatched Fe(110) substrate. The electron energy is 12 eV.

place *h*-BN monolayer on Fe(110) with a lattice match in only one direction, thus being promising for 1D nanopatterning of *h*-BN. The expected strong interfacial interaction between the *h*-BN sheet and the Fe(110) surface may provide a desirable degree of control over the sample geometry and exclude the unwanted element of randomness in the superstructure geometry. Moreover, the strong interfacial interaction between *h*-BN and Fe(110) is promising to achieve a higher degree of the superstructure corrugation than that reported earlier.²⁸ It is also very attractive to use Fe as a cheap substrate material instead of more expensive transition metals. A “washboard” structure of the *h*-BN monolayer on Fe(110) is discovered and characterized by a combination of core-level X-ray spectroscopies, (microbeam) low-energy electron diffraction/microscopy (μ)LEED/LEEM, and scanning tunneling microscopy (STM). The growth mode and domain structure of the interface are examined by low-energy electron microscopy (LEEM). The reported *h*-BN/Fe(110) interface is robust and well ordered, and it has a low defect density, thus representing a prospective platform for growth or distribution of nanoscaled objects in one dimension.

EXPERIMENTAL DETAILS

All samples were prepared in situ in three different experimental stations for X-ray spectroscopy, LEEM, and STM, using the same preparation procedures. Spectroscopic measurements (core-level photoelectron spectroscopy and X-ray absorption) were carried out at the beamline D1011, and LEEM studies were performed in the LEEM/PEEM system (from Elmitec) at the beamline I311 (both at MAX-lab, Lund University), while STM experiments were performed at the Division of Synchrotron Radiation, Lund University. The Fe(110) surface was prepared by epitaxial growth of thick Fe films on a W(110) substrate. The W(110) single crystal was cleaned by several cycles of heating in the oxygen atmosphere ($p(\text{O}_2) = (2-5) \times 10^{-8}$ mbar) at 800–900 °C and subsequent flashing at 1750 °C. The cleanliness of the substrate was verified by photoelectron spectroscopy (PES) and LEED. Iron films with the typical thickness of 20 nm were grown at RT from a commercial evaporator (Omicron EFM3) using an iron rod as a target for e-beam heating. After the deposition, the films were annealed to 600 °C to ensure their smoothness. The quality of the Fe films was checked by the LEED pattern showing only spots related to Fe(110) and by absence of the W 4f signal in PES. The growth of *h*-BN was performed by thermal cracking of borazine ((HBNH)₃) molecules on the hot iron surface at 750–800 °C in the borazine partial pressure of 1×10^{-7} mbar for 5–10 min. Under these

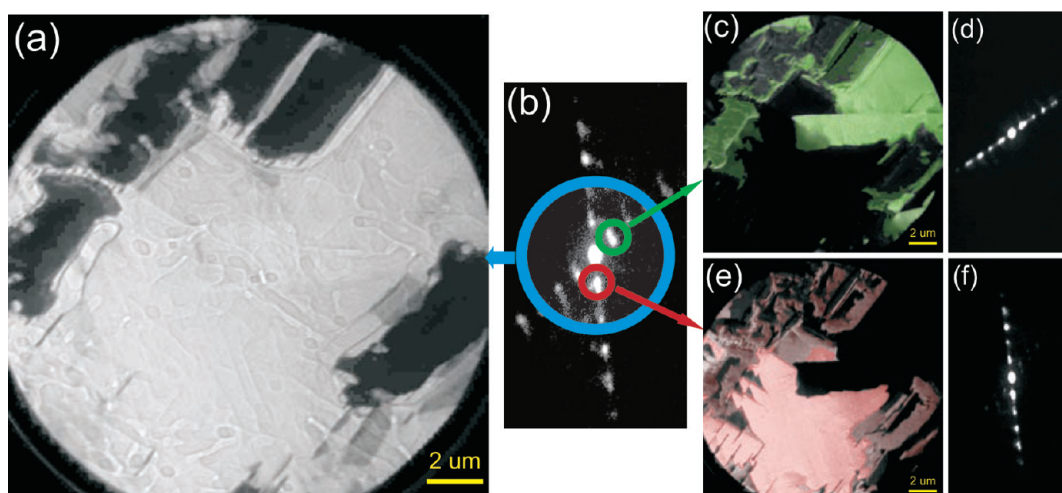


Figure 2. LEEM study of the *h*-BN/Fe(110) sample. An island of the *h*-BN adlayer is imaged in the bright field mode of the LEEM (a), where the electrons contributing to the image are encircled blue in the corresponding μ LEED pattern (b). The same area of the sample imaged with the dark field (DF) mode of the LEEM (c, e), where the only electrons diffracted to the particular spot of the LEED pattern (b), thus escaped from the surface of particular symmetry, make up an image. The size of all images is 20 μ m; the electron energy for both imaging and μ LEED is 12 eV. The spots of the μ LEED pattern (b) used for imaging in the DF mode are highlighted with circles and relations are shown with arrows. The μ LEED patterns (d) and (f) correspond to the two primary domains.

conditions the growth is self-limiting to one monolayer, and no bi- or multilayer contributions to the single layer coverage were observed either spectroscopically or microscopically. The samples were characterized by core-level PES, near-edge X-ray absorption fine structure (NEXAFS) spectroscopy, and LEED. The NEXAFS spectra were measured in the partial electron yield mode, implying a retarding (negative) potential applied at the entrance of the microchannel electron detector. This mode allows cutting off slow secondary electrons with a large escape depth, thus increasing the surface sensitivity and the signal-to-background ratio significantly. The retarding potential U_r of -100 V was used for acquisition of absorption spectra. The photon energy resolution of the N 1s NEXAFS spectra was set to 100 meV; the photon and electron energy resolution of the N 1s photoelectron spectra was 125 meV. Both NEXAFS and PE spectra were accumulated at an angle of 50° between the light polarization plane and the normal to the sample surface, implying in our setup the normal emission geometry. All NEXAFS spectra were normalized to the intensity of the incident radiation; the photoelectron spectra were measured relative to the Fermi level of the corresponding substrate. The FitXPS software²⁹ was used for the peak fit analysis of the PE spectra. The STM measurements were performed at RT in the constant-current operation mode on the samples prepared in a separate chamber equipped with a commercial UHV STM (STM1 from Omicron GmbH). The base pressure in all preparation chambers was better than 2×10^{-10} mbar. The WSxM software³⁰ was used for the STM image processing. Neither filtering nor averaging was applied to the STM images except plane correction.

RESULTS AND DISCUSSION

In Figure 1, LEED patterns for the clean W(110) surface (a), Fe/W(110) (b), and *h*-BN/Fe/W(110) (c, d) are shown. Iron is known to grow epitaxially on W(110) with mostly quasi layer-by-layer mechanism of growth,^{31–33} resulting in large quasi-2D islands of Fe. There is a considerable lattice misfit $\sim 10\%$ between the W(110) surface lattice and that of Fe(110), which leads to the strain in the iron film and to the formation of misfit dislocation network (MDN) inside the film. However, with increasing thickness of the iron film the strain decreases and the MDN-related roughness of the film surface disappears.³³ The LEED pattern corresponding to the MDN was observed in our studies for the films with insufficient

thickness (not shown). Because of this fact only thick enough films with a LEED pattern similar to that depicted in Figure 1b were used for the growth of *h*-BN. In Figure 1c, the LEED pattern from the *h*-BN/Fe(110) sample is shown. The principal spots of the substrate (highlighted with yellow dashed hexagon corresponding to the LEED pattern of the iron film shown in Figure 1b) are accompanied by a number of additional reflexes ordered in crossing lines due to the symmetry of the adlayer-induced moiré superstructure. It should be noted that a twisting of atomic layers in bilayer and trilayer *h*-BN could also result in specific moiré superstructures,³⁴ but the formation of multilayers can be ruled out in our case, as mentioned above. In Figure 1d, the vicinity of the zero-order diffraction spot is shown on a μ LEED pattern taken from the surface area of 1.5 μ m. The nine spots of the adlayer-induced moiré between the principal spots (marked with donut-shaped rings) reflect the periodicity of the superstructure, which can be estimated from the LEED pattern as 2.5 nm.

By using LEEM and μ LEED, we observed that the growth of *h*-BN on Fe(110) begins with the formation of islands with irregular shapes and sizes. A LEEM image of a typical *h*-BN island grown on the Fe(110) substrate is shown in Figure 2a. The *h*-BN monolayer appears as a bright area in the image, while the relief of the surface seen in the image reflects the morphology of the underlying iron film. The μ LEED pattern in Figure 2b was taken from the sample area of ~ 5 μ m. Imaging in the bright-field mode (BF) implies imaging with only those electrons which contribute to the (0,0) diffraction spot and is normally utilized for an overview imaging. To separate domains of different orientation in LEEM, the dark-field (DF) mode is used.³⁵ In the DF mode only electrons accounting for specific nonzero-order spots in the LEED pattern are recorded for imaging. The DF images in Figure 2c,e provide clear evidence for a coexistence of two primary *h*-BN/Fe domains with different spatial orientations, corresponding to the two different sets of LEED reflexes. However, these domains are not fully complementary, as can be seen from a comparison of image (a) with the superposition of images (c) and (e) in Figure 2. To facilitate the comparison, domains of primary orientations are

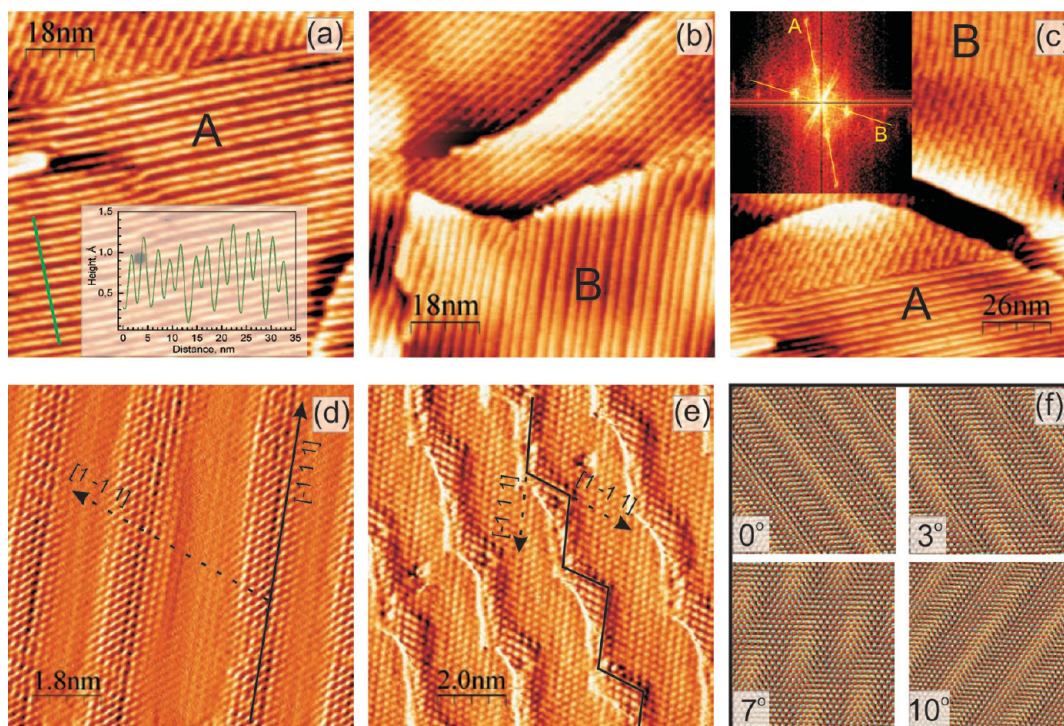


Figure 3. An STM study of the *h*-BN/Fe(110) sample. (a) A typical STM image of the sample. Inset: height profile along the marked line (green). The capital letter A is referred to the major orientation of the imaged superstructure domain. (b) A domain of the second primary orientation (B). Misoriented regions are visible at the top of both images (a) and (b). The size of the images is 90×90 nm, $I_t = 150$ pA, $V_b = 1.2$ V. (c) Coexisting domains A and B together with a misoriented region in between, scan size 130×130 nm, $I_t = 100$ pA, $V_b = 1.2$ V. Inset in the top-left corner is a Fourier transform of image (c). (d) and (e) are high-resolution STM images of atomic rows in the observed structure ($\sim 10 \times 10$ nm, $I_t = 4.7$ nA, $V_b = 0.05$ V). The images (d) and (e) are given in the tunneling current channel. Solid and dashed black lines stand for the crystallographic directions $[\bar{1}11]$ and $[1\bar{1}1]$, respectively, as followed from the atomic model discussed in the text. (f) Model moiré superstructures resulting from a superposition of *h*-BN(0001) and Fe(110) lattices as a function of rotational (polar) angle between them. B, N, and Fe atoms are colored red, blue, and dark yellow, respectively.

colored with saturated green and red in images (c) and (e) of Figure 2, respectively. Slightly misoriented domains deliver worse contrast in the DF images and are marked with faded colors. The partial misorientation of domains can also be seen in the LEED and μ LEED patterns, where the spots are often smeared angularly and radially (see Figure 1d or 2b). It can be a result of a gradual transformation of one primary domain orientation into the other, accompanied by a rotation and stretching of the *h*-BN film. It is also possible to associate patches of misoriented *h*-BN adlayer with a locally increased strain in the underlying iron film because at the *h*-BN growth temperatures (750–800 °C) Fe films can develop local variations in thickness. The μ LEED patterns from the sample areas of ~ 400 nm are shown in Figure 2d,f. These patterns provide further evidence for the existence of two major domain orientations.

Figure 3a shows a typical STM image of the *h*-BN/Fe(110) interface. The topography of the sample is represented by alternating bright protrusions and dark narrow lines. The bright protrusions appear to be lifted above the surface in all the STM images observed, while the dark lines are deeper with respect to the average surface level. Thus, the image shows a wavy corrugation pattern of the *h*-BN monolayer, which can be described as a “washboard”. Remarkably, no defects or kinks of the waves are visible on the step edge (bottom right). The inset in Figure 3a shows a height profile along the green line, revealing a significant degree of *h*-BN corrugation (0.8 Å), while the period of this pattern is ~ 2.6 nm. This value of the *h*-

BN superstructure period is similar to the one obtained from the analysis of the moiré patterns in μ LEED, 2.5 nm. The largest part of the image in Figure 3a shows an area where the *h*-BN film is matched to the substrate along one crystallographic direction, thus constituting a single orientational domain (denoted A). In turn, Figure 3b shows the other orientational domain (denoted B). In the top of Figure 3a,b very characteristic kinky waves are visible. These structures are assigned to those patches of the *h*-BN film which are not aligned with any particular direction of the iron substrate, possibly due to a too fast local growth of the *h*-BN adlayer or poor local quality of the underlying iron film. In Figure 3c, domains A and B are shown together at the bottom and at the top of the image, respectively, while the central part is occupied by the kinky pattern mentioned above, which gradually evolves into the primary domain B. The fast Fourier transform (FFT) of this image (inset in Figure 3c) shows a set of spots ordered in crossing lines. These spots is a signature of the specific moiré superstructure while the crossing is due to the existence of two primary domains with different orientation. The spots in the FFT pattern are slightly smeared due to a contribution of the misaligned area in the center of Figure 3c. Obviously, the FFT pattern in Figure 3c resembles the zero spot LEED pattern from the *h*-BN/Fe sample and gives a plausible explanation of the spot smearing in LEED. Thus, the large-scale STM results are quite consistent with the LEEM and μ LEED findings.

The high-resolution STM images in Figure 3d,e show the atomic-scale structure of the “washboard” corrugation with

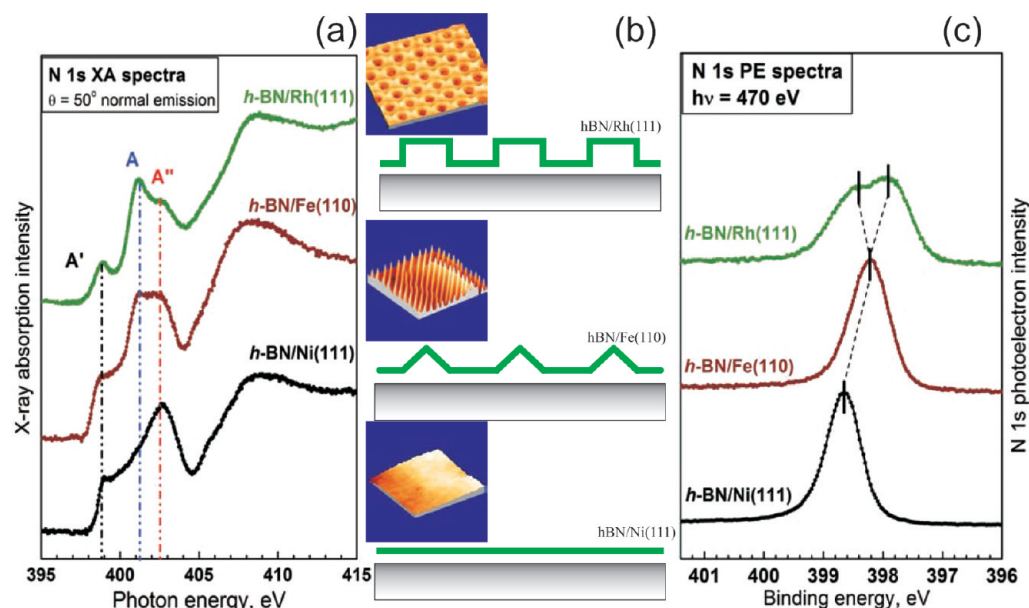


Figure 4. Core-level N 1s NEXAFS (a) and PES (c) spectra from *h*-BN monolayer adsorbed on Fe(110). Corresponding spectra for *h*-BN/Rh(111) and *h*-BN/Ni(111) are shown for comparison. Panel (b) shows a schematic of the *h*-BN adlayer corrugation profile on Rh(111), Fe(110), and Ni(111). Corresponding STM images (own experimental data) are added to panel (b) to clarify the schematics.

straight and kinked nanowaves, respectively. These images are recorded in the STM current channel, representing a map of instant deviation of an actual tunneling current from the preset value. Thus, to a certain extent tunneling current channel in the STM image can be considered as a numerical derivative of the topography image. Even though the spectroscopical information is discarded in this representation, tunneling current channel can provide an increase in the overall sharpness of the image details and enhance the signal-to-noise ratio. Figure 3d,e gives a clear representation of the *h*-BN/Fe short-range atomic structure. The bright spots can be assigned to the centers of *h*-BN rings on the basis of the corresponding topography image (not shown) and the fact that the mean distance between those is ~ 2.5 Å, which matches almost exactly the lattice constant of *h*-BN.³⁶ Figure 3d shows an image of the surface area with a straight “washboard” corrugation pattern, which is the most typical pattern for all the *h*-BN/Fe samples investigated. The actual direction of atomic rows is marked with a black solid line, while the dashed line labels the other possible direction for those due to the substrate surface structure. The crystallographic directions are given with respect to the Fe(110) substrate, on the basis of the moiré superstructure atomic model discussed below, where the *h*-BN film is suggested to be “pinned” along a particular substrate direction. In Figure 3e, the “washboard” corrugation pattern appears kinky, and four successive “waves” are shown. The assignment of the crystallographic directions here is the same as in Figure 3d. However, here the *h*-BN adlayer demonstrates a spontaneous switching in alignment from one to the other lattice-matching direction of the iron substrate. The period of these kinks can vary significantly across the sample surface. This can be understood by looking at the model moiré superstructures presented in Figure 3f, where an unrelaxed atomic lattice of *h*-BN is superimposed on the Fe(110) surface lattice at different rotational angles. In the top-left corner of Figure 3f, the *h*-BN lattice is precisely aligned along the $[1\bar{1}1]$ direction of the substrate. The *h*-BN lattice rotated 3° , 7° , and 10° clockwise with respect to the fixed iron substrate lattice is shown in the

top-right, bottom-left, and bottom-right corners of Figure 3f, respectively. The moiré pattern changes gradually from parallel stripes (when the *h*-BN is lattice matched along the $[1\bar{1}1]$ direction), to a distorted hexagonal pattern (e.g., at 7°), and then back to stripes, this time along the $[\bar{1}11]$ direction (at 10°). The kinky stripes can be then associated with specific moiré patterns, where *h*-BN film is matched along neither $[1\bar{1}1]$ nor $[\bar{1}11]$, e.g., in a transition region between the two primary domains. Rotational misalignment is a common phenomenon for sp^2 -bonded materials weakly adsorbed on transition metal surfaces, for example, graphene on Pt(111)²¹ or *h*-BN on Pd(110).²⁸ Contrary to that, most of the *h*-BN/Fe(110) surface represents a strongly oriented *h*-BN film with an orientation of the corrugation pattern dictated by one of the two major directions while the misaligned transition regions amount to a smaller fraction of it.

It is important to figure out whether the observed 1D periodic structure is a real geometrical “washboard” corrugation or a purely electronic effect resulting from a specific moiré pattern. In principle, an assignment based only on the STM studies may be rather misleading because both surface topography and electronic structure of the sample contribute to the tunneling current variation.³⁷ Nevertheless, in this particular case we consider the observed height variation as a real geometrical corrugation of the *h*-BN sheet because it is observed in all our large-scale topography images recorded with low tunneling current, i.e., with the tip scanning far away from the surface, and in a wide range of bias voltages. At these conditions the influence of the tip on the surface electronic structure is reduced, and the tip probes different fractions of the local density of states. Therefore, the contrast results mainly from the height variations. Besides, the corrugation amplitude observed in STM is rather similar to that reported in the well-known strongly corrugated systems, *h*-BN nanomesh on Rh(111) and Ru(0001).^{3–6,9,38,39}

Further insight into the electronic structure and corrugation of *h*-BN on Fe(110) can be gained by using X-ray spectroscopic techniques. In Figure 4, the N 1s NEXAFS (a) and PE (c)

spectra of this system are shown in comparison with the corresponding spectra from *h*-BN/Rh(111) and *h*-BN/Ni(111). The latter two systems are chosen here for the following reasons. While monolayer *h*-BN is strongly chemisorbed on both Ni(111)^{40,41} and Rh(111),^{7,8,41} it is perfectly lattice-matched on Ni(111)^{42–44} but forms a strongly corrugated 2D nanomesh on Rh(111)^{4,6,11} due to a substantial lattice mismatch. On Fe(110) the strength of chemical interaction is expected to be comparable to the latter case, but the lattice match is possible in only one direction leading to a 1D superstructure. Therefore, in the series *h*-BN/Ni(111)–*h*-BN/Fe(110)–*h*-BN/Rh(111) the monolayer *h*-BN is adsorbed in a sequence “no superstructure”–“1D superstructure”–“2D superstructure”, respectively. Figure 4b shows the corresponding STM images along with the schematics illustrating the morphology of the *h*-BN adlayer in all three cases. The N 1s NEXAFS spectrum from *h*-BN/Ni(111) is dominated by features A–A′–A″ reflecting transitions of the N 1s core electrons to unoccupied states of the π symmetry, of which the strongest details A′ and A″ are due to the Ni 3d–BN π hybridization resulting in a rather strong chemisorption of *h*-BN on Ni(111).^{40,45,46} Feature A, which is the dominating π resonance in the N 1s NEXAFS spectra from both bulk *h*-BN⁴⁷ and weakly interacting *h*-BN monolayer,⁷ can be considered as an indication of nearly noninteracting *h*-BN. Although resonance A is hardly visible in the N 1s NEXAFS spectrum from *h*-BN/Ni, it is quite pronounced in the corresponding spectrum from *h*-BN/Rh(111), thus reflecting the existence of weakly bonded elevated sites in the corrugated *h*-BN nanomesh on Rh(111).⁸ From Figure 4 (a, middle) it is clear that the case of *h*-BN on Fe(110) is somewhat intermediate because resonance A is clearly visible but less pronounced than in the case of *h*-BN/Rh(111). Thus, it is natural to assume a significant corrugation of the *h*-BN sheet, resulting in electronic decoupling of certain sites of the monolayer from the Fe(110) substrate. The area of the nonbonded sites is less than in the case of 2D *h*-BN nanomesh on Rh(111) because the intensity of peak A is smaller in the case of *h*-BN/Fe. This is exactly what is expected in the case of 1D corrugated *h*-BN monolayer. Therefore, the existence of peak A and its relative intensity to the total N 2p(π) NEXAFS signal from *h*-BN/Fe (A′–A–A″) provide evidence for a considerable corrugation of *h*-BN nanowaves on Fe(110). Figure 4c shows N 1s photoelectron spectra from the same samples and in the same order. The spectrum from *h*-BN/Ni(111) is a single line, indicating that all nitrogen atoms are in the same or similar chemical state and the system is highly homogeneous (not corrugated). In contrast, the N 1s PE spectrum from *h*-BN/Rh(111) shows a pronounced splitting in two components separated in binding energy (BE) by $\Delta E_b \sim 0.7$ eV. These components result from the nitrogen atoms in different chemical states, namely highly bonded “pores” (higher BE) and loosely bonded “wires” (lower BE).^{7,8} The N 1s PE spectrum from *h*-BN/Fe(110) (Figure 3c, middle) represents an intermediate situation. On one hand, there is no pronounced splitting typical for a 2D-corrugated *h*-BN monolayer. On the other hand, the line is slightly broadened (from 0.65 eV on Ni to 0.75 eV on Fe) and located on the BE scale between the “wire” and the “pore” signal of the *h*-BN nanomesh. The absence of the second component in the N 1s PE spectrum from *h*-BN/Fe is understandable because in the case of 1D corrugation there are no extended flat regions of “free-standing” *h*-BN, like in the case of 2D nanomesh.

The origin of observed moiré superstructure can be explained on the basis of a simple atomic model presented in Figure 5. It

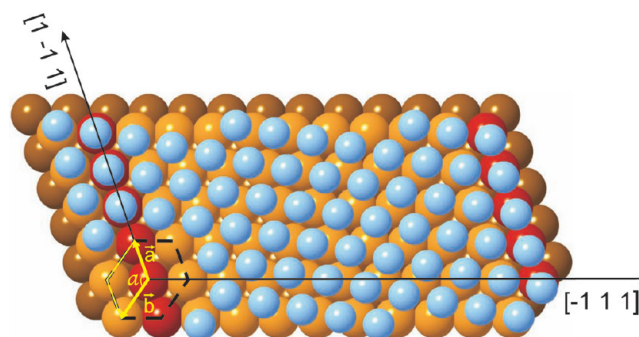


Figure 5. Suggested model of atomic rows direction of *h*-BN on the Fe(110) surface. N atoms are in light blue; Fe atoms are in yellow and brown for the topmost and second layers, respectively. Fe atoms corresponding to the most bonding situations (N in nearly on-top positions) are highlighted in red. For the sake of simplicity, the B sublattice of *h*-BN is omitted.

shows the N sublattice of *h*-BN (blue balls) superimposed onto the Fe(110) surface (yellow and brown balls for the topmost and second from the top layer, respectively). The boron sublattice of *h*-BN is omitted for simplicity. The angle between the equivalent crystallographic directions in the N sublattice is 60°. The Fe(110) surface lattice unit cell is rhombic (shown in the bottom-left corner of the Figure 5a with a yellow line) with the unit cell vectors \vec{a} (length 2.48 Å) and \vec{b} (2.86 Å) and the angle between those vectors $\alpha = 125.3^\circ$. The dashed hexagon underlines the pseudo-hexagonal character of the substrate. There are two equivalent directions in this lattice, i.e., $[\bar{1}11]$ and $[1\bar{1}1]$, where the distance between adjacent Fe atoms (2.48 Å) matches the N-to-N distance in *h*-BN almost perfectly. The on-top positions are expected to be preferable for N adsorption, by analogy with the *h*-BN/Ni(111),^{42–44} *h*-BN/Rh(111),⁶ and *h*-BN/Ru(0001)¹¹ interfaces. An assumption that the most energetically favorable adsorption position for the pair (N,B) is (on-top, fcc-hollow) seems to be rather general for the *h*-BN growth on TM substrates.

The formation of *h*-BN monolayer on Fe(110) can occur along one of these matching directions, $[\bar{1}11]$ or $[1\bar{1}1]$. As the angle between these directions is $\sim 71^\circ$, the *h*-BN monolayer cannot match to the Fe surface in both lattice-matched directions simultaneously. Therefore, if one atomic row of nitrogen sublattice is “pinned” along the $[\bar{1}11]$ direction as shown in Figure 5, the next favorable position for an atomic row of *h*-BN nitrogen atoms in the same direction is shifted 10 Fe–Fe interatomic distances in the $[\bar{1}11]$ direction. In Figure 5, the rows of “pinning” Fe atoms corresponding to the most bonding situations (N in nearly on-top positions) are highlighted in red. It is also obvious that the N positions are not strictly on-top for all “pinning” Fe rows, as N atoms can be shifted along these rows to the bridge positions. However, they are never in the least favorable hollow positions, and adsorption along these rows is still preferable. Also, it is possible that the N atoms do try to fit into the most favorable adsorption positions (still assuming the most stable configuration is (N,B) \rightarrow (on-top, fcc-hollow)), in which case the *h*-BN layer has to undergo a slight side deformation. It can result in a small mismatch between the “pinning” direction on Fe(110) and the direction of the waves and be a reason for certain strain in the *h*-BN film.

This fact can explain the small discrepancy between the direction of atomic rows and the wave direction visible in Figure 3d. Since there are two equivalent crystallographic directions on the Fe(110) surface, it is natural to expect formation of two primary *h*-BN/Fe domains associated with these directions.

CONCLUSIONS

In conclusion, we present a new 1D-nanopatterned structure of *h*-BN adsorbed on the Fe(110) surface, studied by a number of spectroscopic and microscopic techniques. The LEED, μ LEED, and LEEM studies have revealed the presence of two primary domains with a specific 1D moiré pattern, while X-ray spectroscopy and STM have proved the existence of a strong “washboard” corrugation in the *h*-BN film with pronounced wave crests and troughs. The period of this 1D structure is ~ 2.6 nm, and the corrugation amplitude is ~ 0.8 Å; the model of strongly corrugated single layer of *h*-BN is suggested. The reported structure can be used as a robust template for ordering nanoscaled objects in one direction and formation or seeding of nanowires.

AUTHOR INFORMATION

Corresponding Author

*E-mail: alexeip@maxlab.lu.se.

Present Address

[†]Lawrence Berkeley National Lab, Berkeley, CA 94720.

ACKNOWLEDGMENTS

We are grateful for financial support from the Swedish Research Council, the Swedish Foundation for Strategic Research, the Crafoord Foundation, the Knut and Alice Wallenberg Foundation, and the Anna and Edwin Berger Foundation.

REFERENCES

- Barth, J. V.; Costantini, G.; Kern, K. *Nature* **2005**, *437*, 671.
- Ng, M. L.; Preobrajenski, A. B.; Zakharov, A. A.; Vinogradov, A. S.; Krasnikov, S. A.; Cafolla, A. A.; Mårtensson, N. *Phys. Rev. B* **2010**, *81*, 115449.
- Corso, M.; Auwärter, W.; Muntwiler, M.; Tamai, A.; Greber, T.; Osterwalder, J. *Science* **2004**, *303*, 217.
- Berner, S.; Corso, M.; Widmer, R.; Groening, O.; Laskowski, R.; Blaha, P.; Schwarz, K.; Goriachko, A.; Over, H.; Gsell, S.; Schreck, M.; Sachdev, H.; Greber, T.; Osterwalder, J. *Angew. Chem., Int. Ed.* **2007**, *46*, 5115.
- Goriachko, A.; He, Y.; Knapp, M.; Over, H. *Langmuir* **2007**, *23*, 2928.
- Laskowski, R.; Blaha, P.; Gallauner, T.; Schwarz, K. *Phys. Rev. Lett.* **2007**, *98*, 106802.
- Preobrajenski, A. B.; Nesterov, M. A.; Ng, M. L.; Vinogradov, A. S.; Mårtensson, N. *Chem. Phys. Lett.* **2007**, *446*, 119.
- Preobrajenski, A. B.; Vinogradov, A. S.; Ng, M. L.; Čavar, E.; Westerström, R.; Mikkelsen, A.; Lundgren, E.; Mårtensson, N. *Phys. Rev. B* **2007**, *75*, 245412.
- Brugger, T.; Günther, S.; Wang, B.; Hugo Dil, J.; Bocquet, M.-L.; Osterwalder, J.; Wintterlin, J.; Greber, T. *Phys. Rev. B* **2010**, *79*, 045407.
- Song, L.; Ci, L.; Lu, H.; Sorokin, P. B.; Jin, C.; Ni, J.; Kvashnin, A. G.; Kvashnin, D. G.; Lou, J.; Yakobson, B. I.; Ajayan, P. M. *Nano Lett.* **2010**, *10*, 3209.
- Laskowski, R.; Blaha, P. *Phys. Rev. B* **2010**, *81*, 075418.
- N'Diaye, A. T.; Bleikamp, S.; Feibelman, P.; Michely, T. *Phys. Rev. Lett.* **2006**, *97*, 215501.
- Preobrajenski, A. B.; Ng, M. L.; Vinogradov, A. S.; Mårtensson, N. *Phys. Rev. B* **2008**, *78*, 073401.
- N'Diaye, A. T.; Coraux, J.; Plasa, T. N.; Busse, C.; Michely, T. *New J. Phys.* **2008**, *10*, 043033.
- Wintterlin, J.; Bocquet, M.-L. *Surf. Sci.* **2009**, *603*, 1841.
- N'Diaye, A. T.; Gerber, T.; Busse, C.; Mysliveček, J.; Coraux, J.; Michely, T. *New J. Phys.* **2009**, *11*, 103045.
- Marchini, S.; Günther, S.; Wintterlin, J. *Phys. Rev. B* **2007**, *76*, 075429.
- Sutter, P. W.; Flege, J.-I.; Sutter, E. A. *Nature Mater.* **2008**, *7*, 406.
- Coraux, J.; N'Diaye, A. T.; Engler, M.; Busse, C.; Wall, D.; Buckanie, N.; Meyer zu Heringdorf, F.-J.; van Gastel, R.; Poelsema, B.; Michely, T. *New J. Phys.* **2009**, *11*, 023006.
- Loginova, E.; Bartelt, N. C.; Feibelman, P. J.; McCarty, K. F. *New J. Phys.* **2009**, *11*, 063046.
- Sutter, P.; Sadowski, J. T.; Sutter, E. *Phys. Rev. B* **2009**, *80*, 245411.
- Jariwala, D.; Srivastava, A.; Ajayan, P. M. *J. Nanosci. Nanotechnol.* **2011**, *11*, 6621.
- Sicot, M.; Bouvron, S.; Zander, O.; Rüdiger, U.; Dedkov, Yu. S.; Fonin, M. *Appl. Phys. Lett.* **2010**, *96*, 093115.
- Goriachko, A.; He, Y.; Over, H. *J. Phys. Chem. C* **2008**, *112*, 8147.
- Brihuega, I.; Michaelis, C. H.; Zhang, J.; Bose, S.; Sessi, V.; Honolka, J.; Schneider, M. A.; Enders, A.; Kern, K. *Surf. Sci.* **2008**, *602*, L95.
- Allan, M. P.; Berger, S.; Corso, M.; Greber, T.; Osterwalder, J. *Nanoscale Res. Lett.* **2007**, *2*, 94.
- Müller, F.; Hüfner, S.; Sachdev, H. *Surf. Sci.* **2008**, *602*, 3467.
- Corso, M.; Greber, T.; Osterwalder, J. *Surf. Sci.* **2005**, *577*, L78.
- Horcas, I.; et al. *Rev. Sci. Instrum.* **2007**, *78*, 013705.
- Adams, D. L. FitXPS (version 2.12); freely available from <http://www.sljus.lu.se/download.html>.
- Elmers, H. J.; Hauschild, J.; Gradmann, U. *J. Magn. Magn. Mater.* **2000**, *221*, 219.
- Elmers, H. J.; Hauschild, J.; Fritzsche, H.; Liu, G.; Gradmann, U. *Phys. Rev. Lett.* **1995**, *75*, 2031.
- Kolaczkiwicz, J.; Bauer, E. *Surf. Sci.* **2000**, *450*, 106.
- Ci, L.; Song, L.; Jin, C.; Jariwala, D.; Wu, D.; Li, Y.; Srivastava, A.; Wang, Z. F.; Storr, K.; Balicas, L.; Liu, F.; Ajayan, P. M. *Nature Mater.* **2010**, *9*, 430.
- Bauer, E. “LEEM and SPLEEM”, *The Science of Microscopy*; Springer: Berlin, 2007, ISBN 10: 0-387-25296-7 and references therein.
- Cappellini, G.; Satta, G.; Palummo, M.; Onida, G. *Phys. Rev. B* **2001**, *64*, 035104.
- Sautet, P. *Chem. Rev.* **1997**, *97*, 1097 and references therein.
- Laskowski, R.; Blaha, P.; Schwarz, K. *Phys. Rev. B* **2008**, *78*, 045409.
- Preobrajenski, A. B.; Ng, M. L.; Vinogradov, N. A.; Vinogradov, A. S.; Lundgren, E.; Mikkelsen, A.; Mårtensson, N. *Nano Lett.* **2009**, *9*, 2780.
- Preobrajenski, A. B.; Vinogradov, A. S.; Mårtensson, N. *Phys. Rev. B* **2004**, *70*, 165404.
- Preobrajenski, A. B.; Krasnikov, S. A.; Vinogradov, A. S.; Ng, M. L.; Käämbre, T.; Cafolla, A. A.; Mårtensson, N. *Phys. Rev. B* **2008**, *77*, 085421.
- Rokuta, E.; Hasegawa, Y.; Suzuki, K.; Gamou, Y.; Oshima, C.; Nagashima, A. *Phys. Rev. Lett.* **1997**, *79*, 4609.
- Auwärter, W.; Kreutz, T. J.; Greber, T.; Osterwalder, J. *Surf. Sci.* **1999**, *429*, 229.
- Grad, G. B.; Blaha, P.; Schwarz, K.; Auwärter, W.; Greber, T. *Phys. Rev. B* **2003**, *68*, 085404.
- Laskowski, R.; Gallauner, Th.; Blaha, P.; Schwarz, K. *J. Phys.: Condens. Matter* **2009**, *21*, 104210.
- Rusz, J.; Preobrajenski, A. B.; Ng, M. L.; Vinogradov, N. A.; Mårtensson, N.; Wessely, O.; Sanyal, B.; Eriksson, O. *Phys. Rev. B* **2010**, *81*, 073402.
- Preobrajenski, A. B.; Vinogradov, A. S.; Mårtensson, N. *J. Electron Spectrosc. Relat. Phenom.* **2005**, *148*, 59 and references therein.